IOPscience iopscience.iop.org

Home Search Collections Journals About Contact us My IOPscience

Rigid sphere transport through a colloidal gas–liquid interface

This article has been downloaded from IOPscience. Please scroll down to see the full text article.

2010 New J. Phys. 12 023013

(http://iopscience.iop.org/1367-2630/12/2/023013)

View the table of contents for this issue, or go to the journal homepage for more

Download details:
IP Address: 131.211.105.231
The article was downloaded on 26/01/2011 at 14:02

Please note that terms and conditions apply.

New Journal of Physics
The open-access journal for physics

Rigid sphere transport through a colloidal gas–liquid interface

J W J de Folter[1], V W A de Villeneuve[1], D G A L Aarts[2] and H N W Lekkerkerker[1,3]

[1] Van't Hoff Laboratory for Physical and Colloid Chemistry, Utrecht University, Padualaan 8, 3584 CH Utrecht, The Netherlands
[2] Department of Chemistry, Physical and Theoretical Chemistry Laboratory, University of Oxford, South Parks Road, Oxford OX1 3QZ, UK
E-mail: h.n.w.lekkerkerker@uu.nl

New Journal of Physics **12** (2010) 023013 (24pp)
Received 25 September 2009
Published 11 February 2010
Online at http://www.njp.org/
doi:10.1088/1367-2630/12/2/023013

Abstract. In this paper we report on the gravity-driven transport of rigid spheres of various sizes through the fluid–fluid interface of a demixed colloid–polymer mixture. Three consecutive stages can be distinguished: (i) the sphere approaches the interface by sedimenting through the polymer-rich phase, (ii) it is subsequently transported to the colloid-rich phase and (iii) it moves away from the interface. The spheres are covered by a thin wetting film of the colloid-rich phase, to which they are eventually transported. The ultralow interfacial tension in these phase-separating mixtures results in very small capillary forces so that the process takes place in the low Reynolds regime. Moreover, it enables the investigation of the role of capillary waves in the process. Depending on the Bond number, the ratio between gravitational force and capillary force acting on the sphere, different transport configurations are observed. At low Bond numbers, the drainage transport configuration, with a dominant capillary force, is encountered. At high Bond numbers, spheres are transported through the tailing configuration, with a dominant gravitational force. By varying the sphere diameter, we observe both transport configurations as well as a crossover regime in a single experimental system.

[3] Author to whom any correspondence should be addressed.

© IOP Publishing Ltd and Deutsche Physikalische Gesellschaft

Contents

1. Introduction

The transport of rigid objects through fluid–fluid interfaces occurs at a wide range of length scales [1]–[6], ranging from the capture of mineral particles in flotation processes [3] to the migration of magma slabs through the earth's crust [5]. The driving force is usually gravity, but can in principle be any external field. The transport process may be divided into three main stages: (i) approach of the interface, (ii) transport through the interface and (iii) movement away from the interface. The transport configuration by which the sphere breaks through the interface mainly depends on the Bond number $Bo = F_g/F_c \sim \Delta\rho g R^3/\gamma R = \Delta\rho g R^2/\gamma$ [7], where $\Delta\rho$ is the density difference between the sphere and the phase from which it approaches the interface, R is the radius of the sphere, g is the gravitational constant and γ is the interfacial tension between the two phases. The Bond number may be viewed as the ratio between gravitational force F_g and capillary force F_c acting on the sphere. If the sphere density is higher than the density of both phases, $Bo < 1$ and $Bo > 1$ result in the *drainage* and *tailing* transport configurations [7], as illustrated in figure 1. At low Bond numbers, capillary forces dominate and the drainage configuration is observed. Characteristic for this configuration is a thinning film of the first phase (with lower density) between the sphere and the interface, which eventually ruptures, quite similar to droplet coalescence [8, 9]. At high Bond numbers, i.e. a dominant gravitational force, the transport of the sphere proceeds through the tailing transport configuration: the interface deforms strongly on approach of the sphere and the sphere leaves a column or 'tail' of material of the first phase behind, which eventually breaks up into droplets.

From the well-known Reynolds number, we can estimate how important the inertial terms are for these processes compared to viscous dissipation:

$$Re = \frac{\rho u L}{\eta}, \tag{1}$$

with ρ the mass density, u the velocity of the sphere, L the characteristic length and η the viscosity. The balance between gravitational and interfacial forces (Bo) determines the type of transport configuration observed at both low and high Reynolds numbers, although the quasi-static nature of processes at low Reynolds numbers gives very different dynamics from the non-equilibrium dynamics for high Reynolds numbers. The transport of objects through interfaces at high Reynolds numbers has been studied to some extent [6], [10]–[14]. However, in the low Reynolds limit, the configurations that have been studied are quite limited [15]–[17].

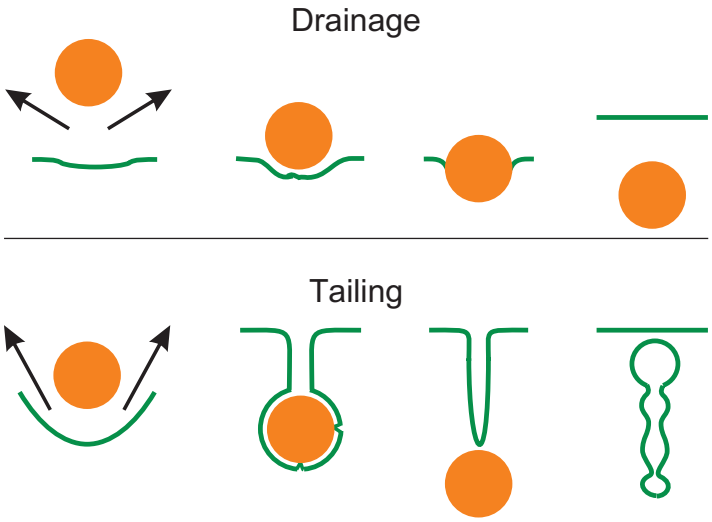

Figure 1. Stages of transport through the drainage ($Bo < 1$) and tailing ($Bo > 1$) configurations.

The scenario of low Re, high Bo transport is especially hard to observe. This can be shown as follows: the characteristic velocity of the interface at low Reynolds numbers is the capillary velocity $u_c \equiv \gamma/\eta$ [18]. By substituting $u = u_c$ and $L = R$ in equation (1), we obtain $Re = \gamma R/(\eta^2/\rho)$. Now for $Bo > 1$ and $Re < 1$, we need the gravitational force F_g to be larger than the capillary force F_c but smaller than the viscous force F_v, i.e. $F_v > F_g > F_c$, which in orders of magnitude corresponds to $\eta^2/\rho > \Delta\rho g R^3 > \gamma R$. As F_g increases with the third power of the sphere radius, this can prove to be quite demanding, with the added complexity that high Peclet numbers $Pe = (\Delta\rho g R^4/kT) > 1$, i.e. diffusion is relatively unimportant, are only obtained for sphere sizes larger than 1 μm. Two possibilities are available to reach the regime: increasing the viscosity or decreasing the interfacial tension. Manga and Stone [17] have reported on sphere transport in this regime using molecular systems with high viscosities. Akers and Belmonte [19] have used a similar approach for a non-Newtonian liquid, which is beyond the scope of the present work.

Here, we access the low Reynolds regime by using a demixed colloid–polymer system with an ultralow interfacial tension. Moreover, the addition of very polydisperse rigid spheres ($R = 2$–$20\,\mu$m) allows for the direct study of both low *and* high Bond number transport within the same experimental system. The interfacial tension has a magnitude proportional to [20, 21]

$$\gamma \propto \frac{k_B T}{d^2}, \tag{2}$$

with $k_B T$ the thermal energy and d the typical length scale at the interface, i.e. the size of the particle. Owing to a depletion-induced attraction [22, 23], these mixtures phase-separate into a colloid-poor, polymer-rich phase and a colloid-rich, polymer-poor phase when the polymer–colloid diameter ratio $q \geqslant 0.30$ [24]. The fluid phases in these colloidal systems exhibit a close analogy with phases in molecular systems. Hence, the polymer-rich phase is often referred to as the 'colloidal gas' or 'gas' phase and, similarly, the colloid-rich phase is called the 'colloidal liquid' or 'liquid' phase. Throughout this paper, we will use these terms

interchangeably. Since colloidal particles have sizes of typically 1–1000 nm, colloidal systems have much lower interfacial tensions—typically of the order of $\mathrm{nN\,m^{-1}}$–$\mu\mathrm{N\,m^{-1}}$ [25]–[29]—than molecular systems.

None of the transport studies consider the capillary forces on the particle during transport, except for studies of spheres attached to a cantilever [30] and studies of sphere tensiometry for determination of the interfacial tension [31]. The focus of these studies, however, is the capture of particles by interfaces without describing the full transport phenomenon, as we do here. Moreover, our system enables us to visualize the break-up of liquid threads that form behind the sphere at high Bond numbers. In studies so far, spheres reached the bottom of the container they were settling in before threads could break up [10]–[12, 17]. In addition, the colloid–polymer system enables the observation of break-up through thermal capillary waves, as we will now discuss.

A special feature of colloid–polymer mixtures is that the typical length and time scales important for interfacial phenomena allow for real-space, real-time investigations of thermal capillary waves [29]. The thermal roughness of the interface is given by $\sqrt{\langle h^2\rangle} \approx k_\mathrm{B}T/\gamma$. The roughness can be visualized for sufficiently low values of interfacial tension ($\approx 10^{-7}\,\mathrm{N\,m^{-1}}$), using laser scanning confocal microscopy (LSCM), as was done previously for droplet coalescence [8] and the pinching of liquid threads [32]. Here, we investigate the effect of these thermal interface fluctuations on sphere transport.

This paper is structured as follows. In section 2 we give a theoretical description of rigid sphere transport through an interface. The experimental system and methods are described in section 3. We present the low Reynolds number, low Bond number transport of a wettable rigid sphere through a colloidal gas–liquid interface, where the drainage transport configuration is observed, in section 4. The tunability of our system is exemplified by the observation of a crossover regime (section 5), where both capillary and gravitational forces are important ($Bo \sim 1$). The scenario for transport at low Reynolds number and high Bond number through the tailing transport configuration is described in detail in section 6. Finally, we summarize our findings in section 7.

2. Sphere transport through interfaces

Consider two liquid phases 1 and 2, see figure 2, with a density difference $\Delta\rho_{12} = \rho_1 - \rho_2$ and each with a viscosity η_n, with $n = 1$ or 2. A sphere with a density difference $\Delta\rho_{rn}$ relative to phase n and radius R sediments in phase 2 at a Stokes velocity $u_\mathrm{s} = 2\Delta\rho_{r2}gR^2/9\eta_2$ towards the interface between the phases. We additionally define z as the gap between the sphere's front and the undeformed interface and d as the interfacial deformation. We set heights in phase 2 as positive.

The sedimentation velocity in phase n results from the equilibrated viscous and gravitational forces F_v and F_g:

$$F_\mathrm{v} = 6\pi\eta_n R u_\mathrm{s} \tag{3}$$

and

$$F_\mathrm{g} = \tfrac{4}{3}\pi R^3 \Delta\rho_{rn} g. \tag{4}$$

For a rigid sphere approaching a free non-deformable surface, exact treatments are given in [33], which describe both the undistorted fall and the velocity close to the surface, where

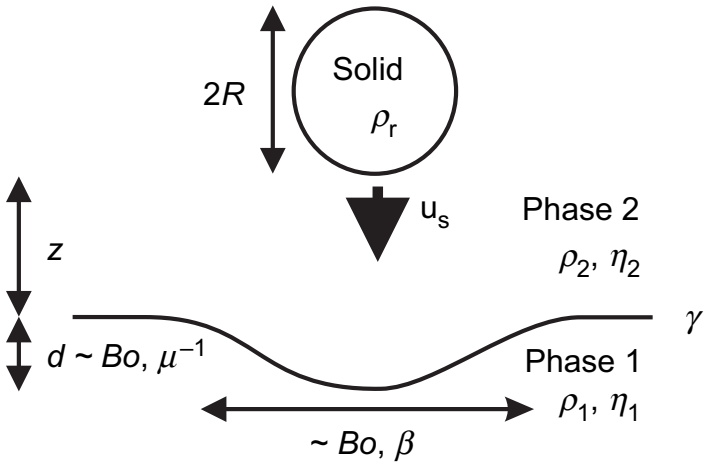

Figure 2. Relevant variables for the transport of a rigid sphere through an interface. The extent of interface deformation d perpendicular to the interface is proportional to Bo and μ (inversely). The width of the deformation depends on Bo and β.

solvent backflow slows the sphere down. Generally, the velocity close to the interface may be written as

$$u_s(\alpha) = \frac{2\Delta\rho_{rn} g R^2}{9\lambda(\alpha)\eta_n}, \tag{5}$$

with λ representing the friction factor, which strongly increases close to the interface:

$$\lambda = \frac{4}{3}\sinh\alpha \sum_{n=1}^{\infty} \frac{n(n+1)}{(2n-1)(2n+3)} C(n,\alpha), \tag{6}$$

with

$$C_{\text{free}}(n,\alpha) = \frac{4\cosh^2((n+1/2)\alpha) + (2n+1)^2\sinh^2\alpha}{2\sinh((2n+1)\alpha) - (2n+1)\sinh(2\alpha)} - 1, \tag{7}$$

with $\alpha = \cosh^{-1}(y/R)$, with y the distance between the centre of the sphere and the interface. In the experiments presented here, we will use this as an approximation as the interface does deform here, and we approximate $y/R \approx (((z+d)/R)+1)$, with $z+d+R$ the distance between the centre of the sphere and the deformed interface.

The departure of the sphere from the interface is similar to the approach at first sight, but there are subtle differences. The solvent backflow at the interface now takes place behind the sphere. Also, instead of a thinning film between the sphere and the interface, the sphere is now moving away from a thickening film between the sphere and the interface.

Following Geller *et al* [7], two scenarios for transport are possible: the drainage and tailing configurations. These authors theoretically investigated the constant velocity and the constant force cases. In the limit of negligible inertial effects, the dimensionless numbers that affect the configuration are Cg, the capillary number Ca and the viscosity ratio between the fluid phases μ:

$$Cg = \frac{u\eta_2}{\Delta\rho_{12} g R^2}, \tag{8}$$

$$Ca = \frac{u\eta_2}{\gamma}, \tag{9}$$

with u the velocity of the sphere, and

$$\mu = \frac{\eta_1}{\eta_2}. \tag{10}$$

Cg and Ca represent the ratio of the viscous stress at the interface relative to buoyancy and surface tension, respectively. High values of Cg result in a relatively broad deformed area along the interface. At high values of Ca, the deformation, both parallel and perpendicular to the interface, becomes large. High values of μ result in a more rigid interface and therefore less interfacial deformation perpendicular to the interface [7]. In our experiments, the constant gravitational force sets the velocity of the sphere far away from the interface and the constant force scenario applies. Since the dimensionless numbers Cg and Ca vary as the sphere slows down upon approaching the interface, we substitute u by $u_s(z = \infty)$ in equations (8) and (9) and Cg becomes the buoyancy ratio β and Ca becomes the Bond number Bo instead, both remaining constant during the transport process. β is given by

$$\beta = \frac{\Delta\rho_{r2}}{\Delta\rho_{12}} \tag{11}$$

and should be larger than unity to prevent the particle from residing at the interface, such as in [15]. For the Bond number, we obtain

$$Bo = \frac{F_g}{F_c} \sim \frac{\Delta\rho_{r2} g R^3}{\gamma R} = \frac{\Delta\rho_{r2} g R^2}{\gamma}, \tag{12}$$

which is the ratio of gravitational force F_g and capillary force F_c. For a sphere the latter is given by

$$F_c = 2\pi\gamma R. \tag{13}$$

At low Bond numbers ($Bo < 1$), the capillary force is dominant and the *drainage* regime is observed. At high Bond numbers ($Bo > 1$), the sphere is transported through the *tailing* transport configuration. Both transport regimes are illustrated in figure 1. We see that the cross-over radius R_{Bo} (for which $Bo = 1$) is equal to

$$R_{Bo} = \sqrt{\frac{\gamma}{\Delta\rho_{r2} g}}. \tag{14}$$

Let us now compare Reynolds numbers for typical molecular and colloidal systems. To this end we write the viscous force, equation (3), as a function of Re by setting $L = R$ and substituting for uR: $F_v \sim Re(\eta^2/\rho)$. Thus, an inertial force of at least η^2/ρ is required to enter the high Re regime. For the transport, the relevant inertial forces are the capillary force ($\sim\gamma R$) and the gravitational force ($\sim\Delta\rho g R^3$). To estimate the magnitude of the forces involved, we insert typical values for studies in molecular systems (table 1). Consider a sphere with a radius $R \sim 10^{-3}$ m, with a density difference with the surrounding fluid $\Delta\rho_{r2} \sim 10^2$ kg m^{-3}, moving towards an interface with interfacial tension $\gamma \sim 10^{-2}$ N m^{-1}. The fluid has a density $\rho \sim 10^3$ kg m^{-3} and a viscosity $\eta \sim 10^{-3}$ Pa s. Consequently, $\eta^2/\rho \approx 10^{-9}$ N. The capillary and gravitational forces are of the order of 10^{-5} and 10^{-6} N, respectively. Compared to η^2/ρ, this is much too large to end up in the low Reynolds regime. It is particularly difficult to bring the capillary force to the low Reynolds regime, since it only depends on R, compared to R^3 for

Table 1. Comparison of characteristic interfacial and sphere transport quantities for colloid–polymer and molecular systems.

	Quantity	Unit	Colloid–polymer	Molecular
Interfaces				
Interfacial tension	γ	$\mathrm{N\,m^{-1}}$	10^{-7}	10^{-2}
Interface roughness	$L_T = \sqrt{\langle h^2 \rangle}$	m	10^{-7}	10^{-10}
Viscosity	η	Pa s	10^{-2}	10^{-3}
Sphere transport				
Density difference	$\Delta\rho_{rn}$	$\mathrm{kg\,m^{-3}}$	10^{2}	10^{2}
Typical sphere radius	R	m	10^{-5}	10^{-3}
Crossover radius	R_{Bo}	m	10^{-5}	10^{-3}
Viscous force	η^2/ρ	N	10^{-7}	10^{-9}
Capillary force	γR	N	10^{-12}	10^{-5}
Gravitational force	$\Delta\rho g R^3$	N	10^{-12}	10^{-6}
Dimensionless numbers				
Bond number	Bo		10^{0}	10^{-1}
Reynolds number	Re		10^{-5}	10^{3}

the gravitational force. In such systems, the low Reynolds regime is only obtained for particle radii of $R = 10^{-7}$ m. These particles are clearly Brownian and the transport process for such particles is presently inaccessible by microscopic methods. Nearly all other studies on high Bond numbers are therefore necessarily at high Reynolds numbers too. To our knowledge, the only experimental low Reynolds number, high Bond number study was performed by Manga and Stone [17], using molecular systems with high viscosities.

We reach the low Reynolds regime through the ultralow interfacial tension in demixed colloid–polymer mixtures, and by the use of relatively small spheres ($R \sim 10^{-5}$ m). If we insert typical values for colloid–polymer mixtures, see table 1, we find that the capillary and gravitational forces are now of the order of 10^{-12} N, much lower than $\eta^2/\rho \sim 10^{-7}$ N. Evidently, we have accessed the low Reynolds regime. Since the crossover radius $R_{Bo} \sim 10^{-5}$ m, both low and high Bond numbers can be visualized by varying the size of the sphere.

3. Experimental system and method

The transport of rigid spheres was studied in three different phase-separated colloid–polymer systems. The dispersions consist of fluorescently labelled poly(methyl-methacrylate) spheres [34], suspended in *cis–trans* decalin, with polystyrene added as a depletant polymer to induce attraction. The first system was fluorescently labelled with 7-(diethylamino)-coumarin-3-carboxylic acid *N*-succinimidyl ester coupled with 4-aminostyrene (CAS), the other two with 4-methylaminoethyl methacrylate-7-nitrobenzo-2-oxa-1,3-diazol (NBD-MAEM). The respective radii of the colloids R_c were 69, 25 and 71 nm, as determined by dynamic light scattering, with a particle polydispersity of approximately 10% from scanning electron microscopy. The radii of gyration R_g of the polystyrene polymers were estimated [35] to be 42, 14 and 43 nm, respectively. We will refer to the respective systems as System IA or IB (depending on the state point A or B in the phase diagram; see figure 3(a)), System II and System III.

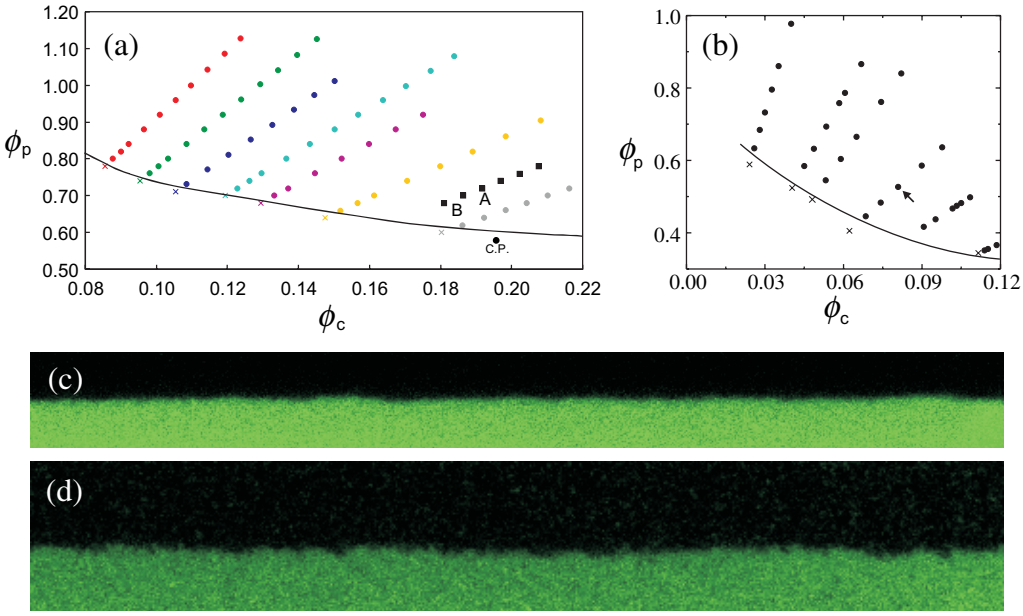

Figure 3. Phase diagrams as constructed by dilution lines for (a) System I and (b) System II. Filled circles indicate state points where phase separation occurs, crosses indicate state points in the one phase region. The binodal (black line) is a guide to the eye. State points at which measurements were performed are indicated by (a) letters or (b) an arrow. The phase diagram of System III is not shown, but was constructed similarly. (c) LSCM image of the equilibrated gas–liquid interface for System IA of $100 \times 10.0\,\mu$m. (d) LSCM image of the equilibrated gas–liquid interface for System IB of $103 \times 15.9\,\mu$m.

The size ratio $q = R_g/R_c \approx 0.6$ in the used systems allows for the coexistence of a polymer-rich, colloid-poor (colloidal gas) phase and a colloid-rich, polymer-poor (colloidal liquid) phase. Phase diagrams were constructed by repetitive dilution of several phase-separating samples. State points were prepared depending on their colloid volume fraction $\phi_c = \frac{4}{3}\pi R_c^3 n_c$ and polymer volume fraction $\phi_p = \frac{4}{3}\pi R_g^3 n_p$, where n_c and n_p are the number densities of colloids and polymers, respectively. The phase diagrams for Systems I and II are shown in figures 3(a) and (b). System I was studied with an Axiovert 200M Zeiss microscope mounted with an LSM5 Exciter scanhead, with the focal plane parallel to the direction of gravity. The microscope was furthermore equipped with an Ar laser with both a 458 nm and a 488 nm line and a Zeiss 60× CFI Plan Apochromat (NA 1.4) lenses. The capturing rate was approximately five frames (512×512 pixels) per second. Figures 3(c) and (d) show images of the equilibrated colloidal gas–liquid interface for state points in System I at which low and high Bond number sphere transports were studied, respectively. It is clear that the interface is corrugated by fluctuations in height due to thermal energy, called capillary waves, which become more pronounced on going from state point A to B (γ decreases). Systems II and III were studied with a Nikon Eclipse E400 microscope mounted with a Nikon C1 scanhead, again with the focal plane parallel to the direction of gravity. The capturing rate was approximately one frame (512×512 pixels) per second. The microscope was furthermore equipped with a 488 nm ArKr laser and Nikon 20× ELWD Plan Fluor (NA 0.45) and Nikon 60× CFI Plan Apochromat

(NA 1.4) lenses. In both cases, the sample container is a small glass vial, part of which is removed and replaced by a thin (0.17 mm) glass wall. Very large, very polydisperse PMMA-NBD spheres ($R = 50$ nm–50 μm, $\rho_r = 1.17\,\mathrm{g\,ml^{-1}}$) were obtained from a synthesis following [34], and subsequently size-fractionated twice in hexane. The resulting spheres with $R = 2$–20 μm were transferred to *cis–trans* decalin and diluted to a concentration of 1 wt%. A small amount of these spheres (less than 10 μl or 1.0% (v/v) of the total sample volume) was carefully added to the top of the colloidal gas phase, after $\sim$16 h of equilibration of the sample to complete phase separation. The material was either added with a pipette or injected through a thin plastic tube. The spheres subsequently sedimented towards the gas–liquid interface and moved through it. During sedimentation in the gas phase, the spheres were covered by a thin wetting film of liquid phase. All the capillary events during transport occur through interactions between the film on the sphere and the macroscopic interface between the phases. We therefore ignore the interfacial tension between the surface of the sphere and the surrounding phases and consider the interfacial tension between the two colloidal phases for all transport events.

A powerful aspect of this study is that all relevant system variables may be determined by microscopy. To this end we determine the bulk sedimentation velocities of the spheres and the capillary wave height–height positional and time correlation functions $g_\mathrm{h}(t)$ and $g_\mathrm{h}(x)$. These provide enough information to determine the interfacial tension γ as well as the mass densities ρ_g and ρ_l and viscosities η_g and η_l (subscripts 'g' and 'l' denote the colloidal gas and liquid phases). The bulk sedimentation velocities give $(\rho_r - \rho_\mathrm{l})/\eta_\mathrm{l}$ for the liquid phase and $(\rho_r - \rho_\mathrm{g})/\eta_\mathrm{g}$ for the gas phase. The interfacial tension γ follows directly from both correlation functions. The capillary length, obtained from $g_\mathrm{h}(x)$ or the interfacial profile at the wall [28, 36], may be used to extract $\rho_\mathrm{l} - \rho_\mathrm{g}$. The dynamic correlation function $g_\mathrm{h}(t)$ provides a measure of the capillary time, from which $\eta_\mathrm{l} + \eta_\mathrm{g}$ is deduced. Thus, we have four equations with four unknowns, which can be solved.

In figures 4(a) and (b), the quantities $\sqrt{u_\mathrm{s}}$ in, respectively, the gas and liquid phase are shown as a function of sphere size for System I. There is a linear relation between the two quantities, indicating that the fluids behave like Newtonian fluids at the shear rates applied by the spheres, which are of order $u_\mathrm{s}(z = \infty)/2R$. The positional and time correlation functions for capillary waves $g_\mathrm{h}(x)$ and $g_\mathrm{h}(t)$ for System I are shown in figures 4(c) and (d). For comparison, the viscosities and densities of a state point similar to System IA and the state point studied in System II were determined with a DMA 5000a density meter and an Anton Paar Physica MCR300 rheometer. These methods require much sample volume and are destructive, but provide a check on the quality of the data obtained from microscopy.

Table 2 gives an overview of the physical properties of the transport systems determined by both methods. For System II, there is excellent agreement between the values obtained by both methods. For System IA, the values are somewhat different, but show the correct tendency since the state point studied by microscopy is slightly closer to the critical point than the sample studied using the more conventional methods. This gives confidence for the reliability of the values measured for Systems IB and III.

Systems IA and II with high R_{Bo} will be used to study the low Bond number limit, and Systems IB and III with low R_{Bo} will be used to study the high Bond number limit. Furthermore, a crossover regime is observed in Systems IB and III. Clearly, we may compare the results in the systems for variation of Bo. Where possible and relevant, we will compare between values for μ or $\sqrt{\langle h^2 \rangle}$, while keeping β (almost) constant.

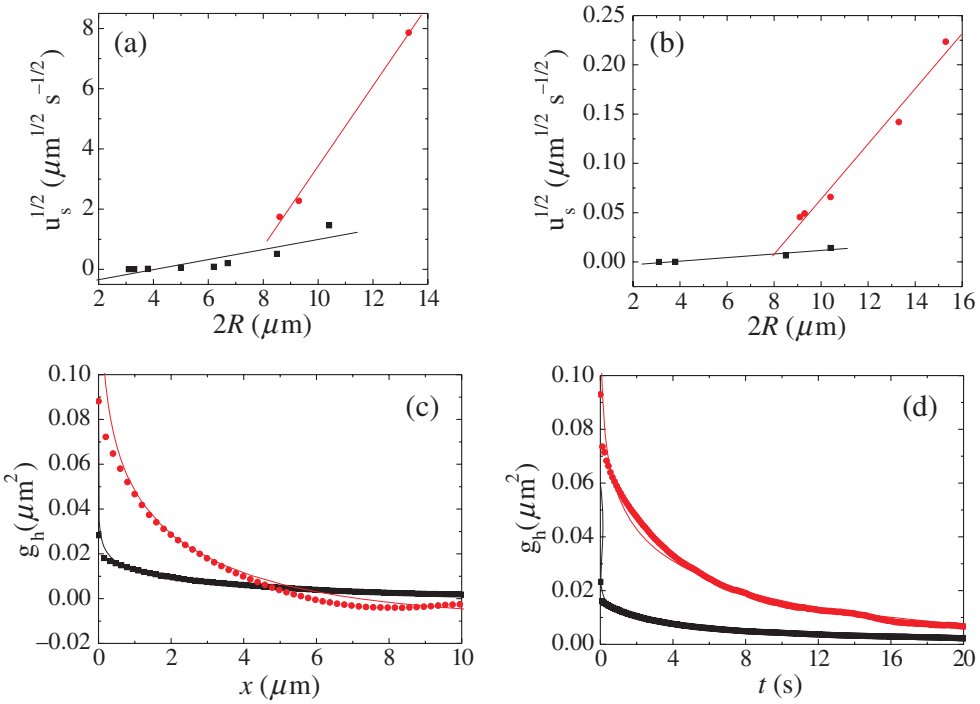

Figure 4. Determination of the physical properties for System I from microscopy. Squares represent the measured data for state point A, circles those for state point B. (a) Determination of $\Delta\rho_{rg}/\eta_g$ from spheres sedimenting in the colloidal gas phase. Data for Systems II and III are not shown. (b) Determination of $\Delta\rho_{rl}/\eta_l$ from spheres sedimenting in the colloidal liquid phase. (c) Determination of γ and $\Delta\rho_{lg}$ from the static correlation function $g_h(x)$. For System II, we determined the capillary length from the profile at the wall (not shown). (d) Determination of γ and $\eta_l + \eta_g$ from the dynamic correlation function $g_h(t)$.

Table 2. Physical properties of the systems studied obtained from microscopy and rheometer and density meter experiments. Values from the latter two are given in parentheses.

		System			
Quantity	Unit	IA	IB	II	III
ρ_l	kg m^{-3}	964 (989)	930	943 (942)	957
ρ_g	kg m^{-3}	892 (887)	906	893 (889)	931
η_l	mPa s	87 (105)	60	35 (31)	25
η_g	mPa s	13 (6)	6	10 (8)	6
R_{Bo}	μm	8 (8)	3	7 (7)	4
γ	nN m^{-1}	140	24	160	45
$\sqrt{\langle h^2 \rangle}$	μm	0.12	0.32	0.065	0.10
Re	–	10^{-6}	10^{-6}	10^{-6}	10^{-6}
Bo	–	0.1–1	1–34	0.1–1	1–10
β	–	3.8 (2.7)	9	5.2 (5.2)	9
μ	–	6.7 (13)	10	3.3 (3.8)	4

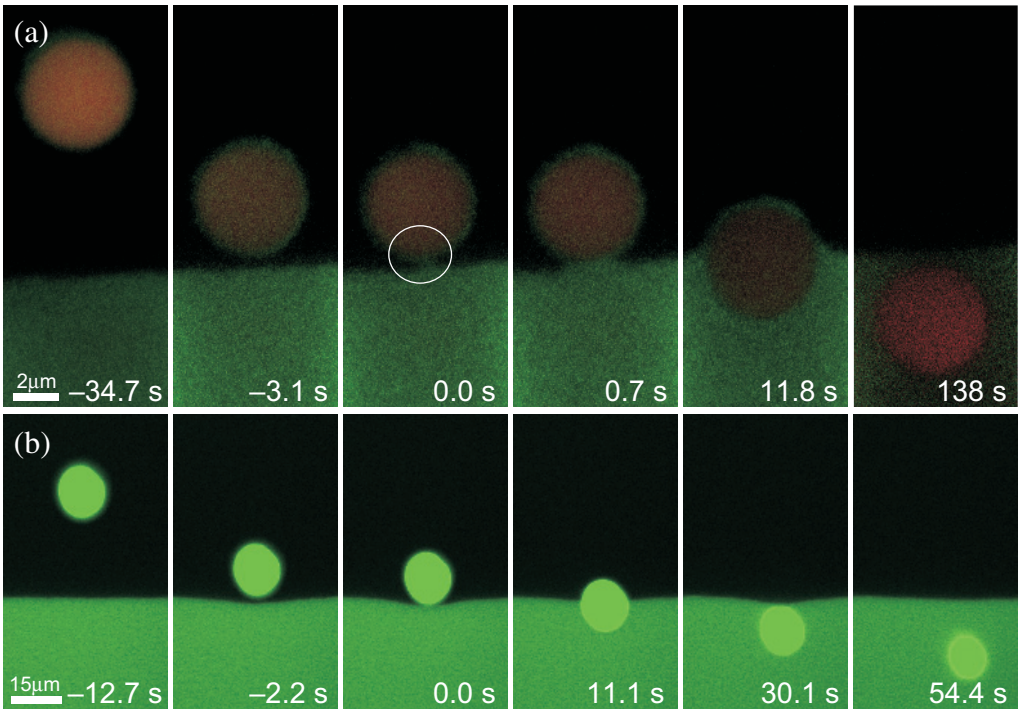

Figure 5. Stages of transport through the drainage mode in (a) System IA and (b) System II. The formation of the initial connection between the interface and the wetting film on the sphere is set as $t = 0$. (a) Series of LSCM images for the transport of a 5.0 μm diameter sphere ($Bo = 0.12$). We can clearly distinguish the approach stage, the formation of a connection through capillary waves, the transport of the sphere through the interface by the growth of the neck and the movement away from the interface. See Movie 1, available at stacks.iop.org/NJP/12/023013/mmedia. (b) Same as in (a), but now for a 15.5 μm diameter sphere ($Bo = 1.0$). Here, the interface clearly deforms during the approach and before the sphere detaches from the interface. The interface recovers after detachment. The resolution in time is less than in (a) and the effects in the wetting film are less obvious because the dyes of the sphere and the colloids are identical. See Movie 2, available at stacks.iop.org/NJP/12/023013/mmedia.

4. Drainage mode

At low Bond numbers ($Bo < 1$), spheres are transported through the drainage transport configuration. Characteristic images of all stages are shown for spheres with diameters of 5.0 μm (System IA, figure 5(a)) and 15.5 μm (System II, figure 5(b)) and Bond numbers of 0.12 and 1.0, respectively. When sedimenting in the polymer-rich phase, a wetting film of the colloid-rich phase is present around the sphere, as can be clearly seen in (the coloured version of) figure 5(a). This layer is acquired when the spheres are added and pass through the air–colloidal gas interface, where colloidal liquid phase is present [32] and wets the incoming rigid sphere. Due to the depletion interaction, the sample wall may be wetted by the colloidal liquid as well [37]; therefore, it is not surprising that this layer is also stable for the curved particle surface. Interestingly, as for the interface between the bulk gas and liquid phase, we are able to visualize thermally induced capillary waves on the wetting layer.

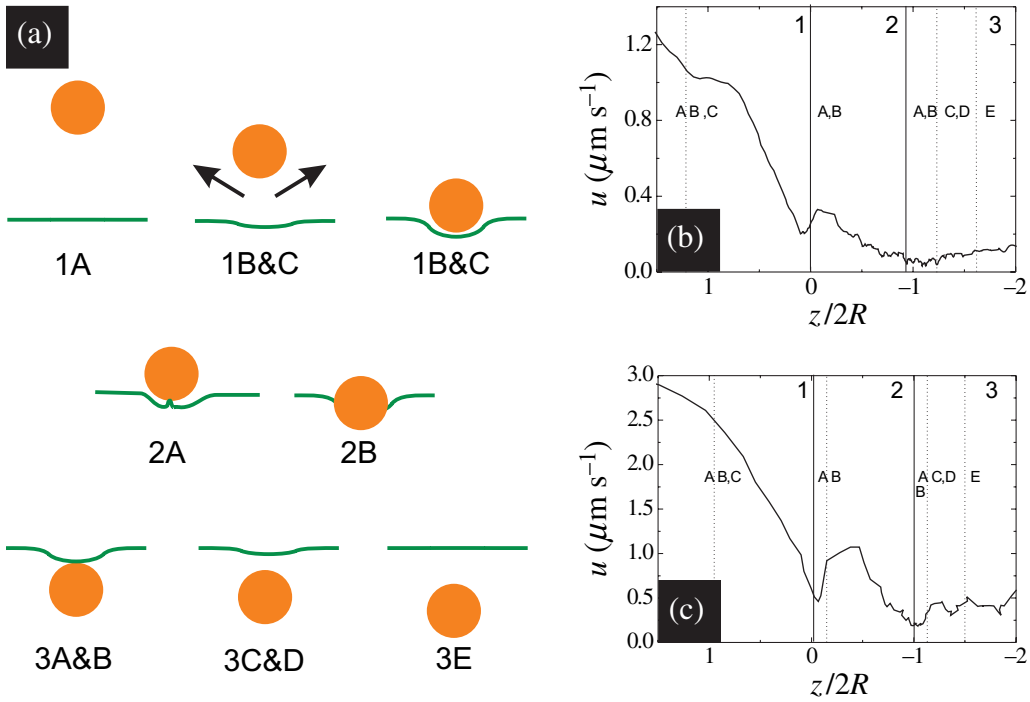

Figure 6. (a) Subdivision of the (1) approach, (2) transport and (3) moving-away stages in events for the drainage transport configuration. The same labelling is used in the text. (b) Drainage velocity profile during transport of a 10.4 μm diameter sphere ($Bo = 0.52$) in System IA. Solid lines separate the stages, whereas dotted lines indicate transitions between the events. Numbers and letters refer to the events as assigned in (a). (c) Similar to (b) for the 15.5 μm diameter sphere ($Bo = 1.0$) in System II shown in figure 5(b).

We now describe the transport process for the drainage configuration by subdividing the approach, transport and moving-away stages in 10 events. These are schematically illustrated in figure 6(a). Far away from the interface, the sphere sediments at constant velocity in the gas phase (1A), until the distance to the interface becomes approximately one sphere diameter. Closer to the interface, the sphere slows down (1B) and—for relatively large spheres—the interface deforms (1C). The extent of deformation is the result of the interplay between gravity-induced solvent backflow and capillary forces. The draining film of gas phase between the sphere and the interface becomes thinner, until the capillary waves of the interface and those on the wetting film around the sphere connect (2A). Subsequently, this connection grows as the sphere is dragged through the interface by capillary forces (2B). The interfacial area between the colloidal gas and liquid phase minimizes as the wetting film on the sphere merges with its bulk phase. Minimization of interfacial area is therefore the driving force of this stage of the process. When the sphere is fully immersed in the liquid phase, the sphere may again deform the interface (3A), it detaches from it by gravity (3B) and accelerates (3C) towards its bulk sedimentation velocity in the liquid phase (3E), while the interface regains its initial flat shape (3D). We will discuss the transport stage in more detail first, followed by the approach and moving-away stages. Figures 6(b) and (c) show the characteristic velocity profiles for the transport of spheres in Systems IA and II, respectively. The velocity is shown as a function of z,

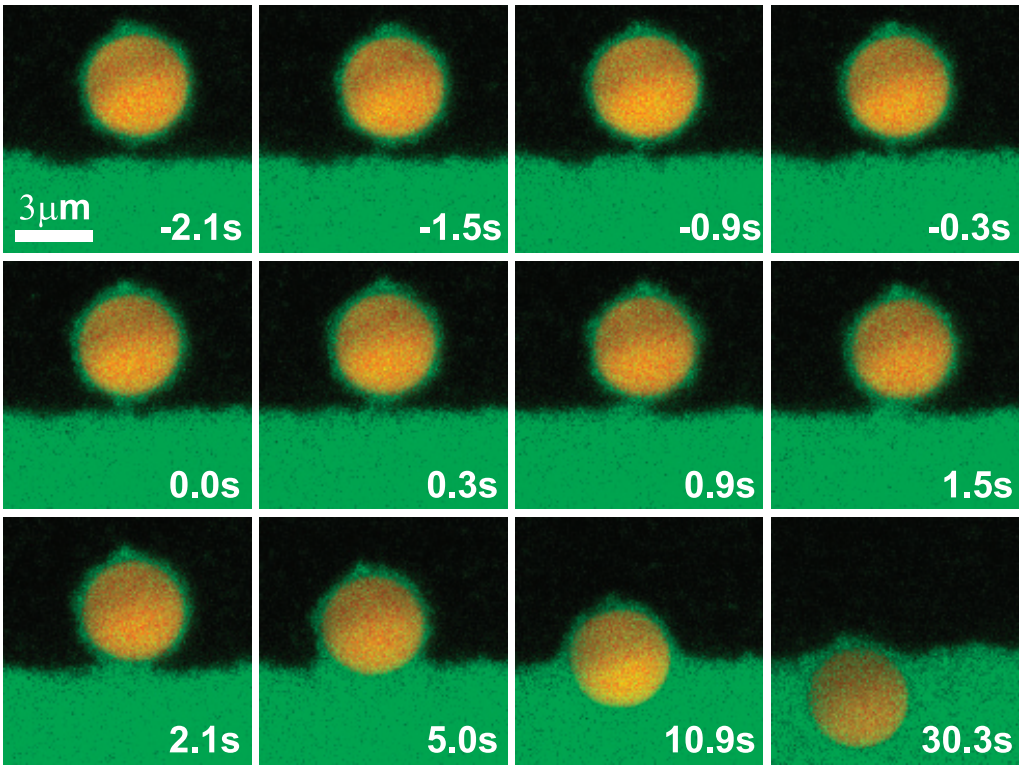

Figure 7. Transport of a 4.4 μm diameter sphere ($Bo = 0.09$), covered with a wetting film, through the interface of System IA. Initially, the capillary waves on the interface and the wetting film are not close enough to create a connection. However, when the fluctuations exceed the interface–film spacing, a connection is formed (at $t = 0$ s). This occurs at a separation of roughly twice the root mean square interface roughness $\sqrt{\langle h^2 \rangle}$. Subsequently, the neck of the connection grows and the sphere is dragged through the interface into the liquid phase by capillary forces. See Movie 3, available at stacks.iop.org/NJP/12/023013/mmedia.

made dimensionless with the sphere diameter. The velocity of the sphere decreases strongly as the sphere approaches the interface. Subsequently, the sphere accelerates while it is transported through the interface by capillary forces. After transport the sphere resides close to the interface for a while and finally accelerates to a bulk sedimentation velocity in the liquid phase.

The transport of a sphere in the draining film configuration is initiated by the formation of a connection between the wetting film of liquid phase on the sphere and the interface, and proceeds with the passage of the sphere through the interface by capillary forces. In figure 7, we show these events for a 4.4 μm diameter sphere ($Bo = 0.09$) in System IA. The time at which the connection is made is set as $t = 0$. The creation of the connection between the wetting film on the sphere and the interface is clearly mediated by capillary waves on both the wetting film and the interface. In the limit of a motionless sphere, the time before two fluctuations cover a wetting film–interface separation Δ is expected to depend on the mean square interfacial roughness $\langle h^2 \rangle$. Indeed, the separation between the film and the interface at which the connection is made is approximately 200 nm, which roughly corresponds to $2\sqrt{\langle h^2 \rangle}$ (~ 240 nm). After the connection is made, the sphere is dragged into the liquid phase while the connection grows rapidly.

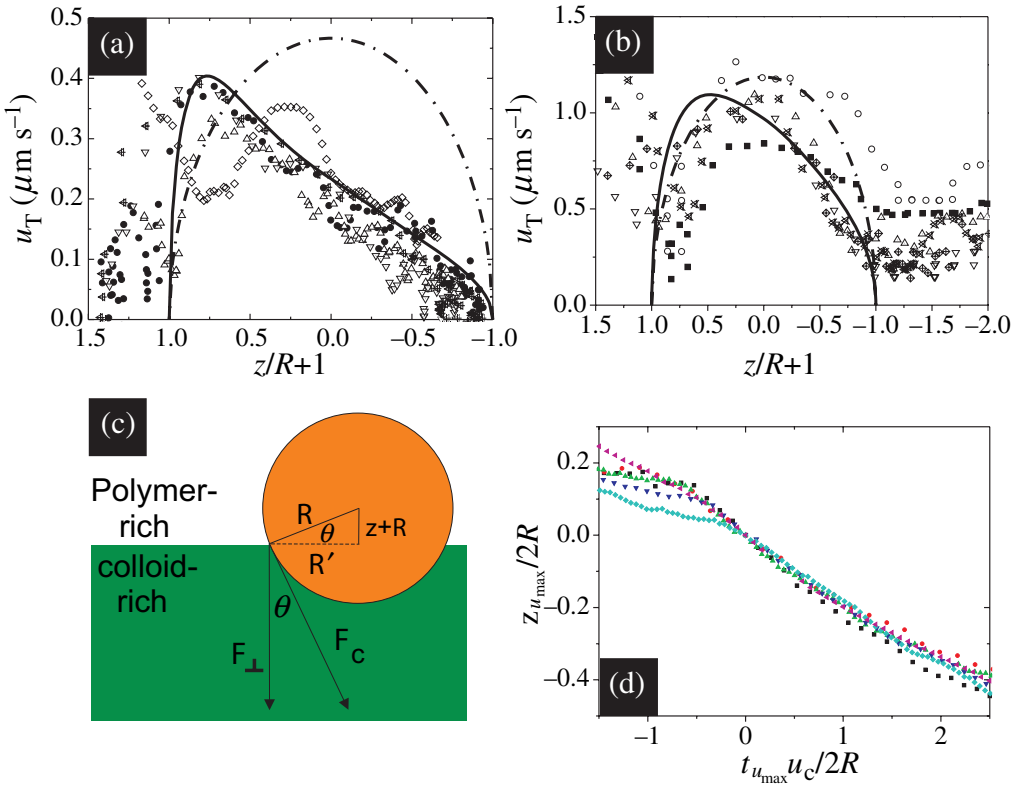

Figure 8. Transport at low Bond numbers of spheres with various sizes. Panels (a) and (b) show the velocity profiles for the transport of spheres through the interface in, respectively, Systems IA ($Bo = 0.05$–0.52; 3.1–10.4 μm diameter) and II ($Bo = 0.55$–1.17; 11.3–16.5 μm diameter) as a function of $(z/R) + 1$. The lines correspond to the model described in (c). (c) Schematic illustration of the transport of the sphere through the interface. The sphere is dragged down by the component $F_\perp$ of the capillary force F_c that is perpendicular to the interface. The angle θ of $F_\perp$ relative to F_c hence determines the transport velocity. F_c is parallel to the curvature of the sphere at the interface height (complete wetting); thus $\cos\theta = R'/R = a$. (d) Dimensionless height versus time for the data shown in (a).

The connection is made at the centre of the bottom part of the sphere, where minimum separation occurs. For spheres that deform the interface more strongly, the required minimum separation for film coalescence may occur at the side of the deformed area. This is the case for high Bond numbers (next sections), for droplets (low Bo) in droplet coalescence [8] and for low Bond number spheres in molecular systems, where $\sqrt{\langle h^2 \rangle}$ is much smaller [15]. The crossover between the two types of events is determined by $\sqrt{\langle h^2 \rangle}$ and R_{Bo} (at fixed β and μ).

During transport, the viscosity experienced by the sphere rises substantially because of the high viscosity contrast μ between the phases in System IA. This is clear in figure 7. Immersion up to the radius of the sphere takes approximately 10 s, whereas full immersion takes an additional 20 s. In System II with low μ, both events occur in roughly the same amount of time. The transport velocities are shown for a range of Bond numbers in figure 8(a) (System IA)

and figure 8(b) (System II). Figure 8(a) has a higher time resolution. We scale $z+R$ with the sphere radius R and $z=0$ is the undeformed interface position. An increase in velocity starts at $(z/R) \approx 2\sqrt{\langle h^2 \rangle}$ for smaller spheres, thus roughly corresponding to the critical distance at which capillary waves on the wetting film of the sphere and the interface start to connect. For larger spheres, the interface deforms and the acceleration of the sphere consequently occurs at lower (z/R).

The most striking feature is perhaps that the maximum transport velocity $u_{\mathrm{T,max}}$ does not depend on the sphere size. In the quasi-static limit of the Navier–Stokes equation, we may equate the viscous drag force $F_{\mathrm{v}} = 6\pi\eta R u$ with the capillary force $F_{\mathrm{c}} = 2\gamma R \cos\theta$ as sketched in figure 8(c). This results in an instantaneous transport velocity $u_{\mathrm{T}}(a)$:

$$u_{\mathrm{T}}(a) = \frac{1}{3}\frac{\gamma}{\eta_{\mathrm{eff}}(a)}\sqrt{1-a^2}, \tag{15}$$

with $a = z/R+1$ and η_{eff} the effective viscosity, which is a complex function of a. Clearly, it also depends on interfacial deformation and therefore on Bo, β and μ. Since the connection is made between the interface and the wetting film, we may use the gas–liquid interfacial tension γ. By approximating $\gamma/\eta_{\mathrm{eff}} = \gamma/(\eta_1+\eta_2) \approx u_{\mathrm{c}}$, with u_{c} the capillary velocity, we find $u_{\mathrm{T,max}} = u_{\mathrm{c}}/3 = 0.47\,\mu\mathrm{m\,s^{-1}}$, which agrees well with the directly obtained value of $u_{\mathrm{T,max}} = 0.41\,\mu\mathrm{m\,s^{-1}}$ for System IA. For System II, the lower resolution in time results in less accurate velocities, but we nonetheless find $u_{\mathrm{T,max}} = u_{\mathrm{c}}/3 = 1.2\,\mu\mathrm{m\,s^{-1}}$ compared to the experimental $u_{T,\mathrm{max}} = 0.9$–$1.1\,\mu\mathrm{m\,s^{-1}}$. The curves for u_{T} are shown as dashed lines in figures 8(a) and (b). The shape of the profile and the location of $u_{\mathrm{T,max}}$ are well predicted by using an effective viscosity based on the relative amount of interfacial area between the sphere and each of the phases. However, prefactors (from fitting) of 0.25 (IA) and 0.4 (II) are still needed for more quantitative agreement (solid curves in figures 8(a) and (b)).

We are able to scale the transport stage for variation of the Bond number ($Bo < 1$) within both experimental systems, by defining $t_{u_{\mathrm{T,max}}} = 0$ and height $z_{u_{\mathrm{T,max}}} = 0$ as the time and height at which $u_{\mathrm{T,max}}$ occurs, and scaling position and time we obtain the 'master curves' for Systems IA (figure 8(d)) and II (not shown), which are thus only valid for given values of μ and β.

We now describe the approach and moving-away stages. The approach of the sphere towards the interface was already discussed in detail in [38] for System II. Here, we combine these results with data from System IA. Far away from the interface all spheres sediment at constant velocity. They start to slow down due to solvent backflow at a separation between sphere and interface of about their own diameter. Moreover, the interface starts to deform for larger spheres, with sizes increasing up to R_{Bo}, as the gravitational force becomes more important. On further approach, the velocity continues to decrease strongly and the interface distortion becomes more pronounced. In figure 9(a), we show the master curves for the approach with scaled heights and times. Note that the spheres studied in System IA—in comparison with System II—may be followed up to smaller values of $(z+d)/2R$ due to the higher image resolution. The approach curves are very well described by the theoretical approach of a sphere towards a free, non-deformable interface equation (5) [38] (solid line in figure 9(a)). For System IA, we are able to observe deviations from the theoretical curve, which start to take place at $(z+d) \approx 2\sqrt{\langle h^2 \rangle}$, when capillary waves become important. Furthermore, fluctuations show up in the approach curve for spheres that visibly display Brownian motion ($Bo < 0.1$).

After transport of the sphere through the interface, gravity becomes the dominant driving force for the downward movement of the sphere again. In this phase, the data of System II are

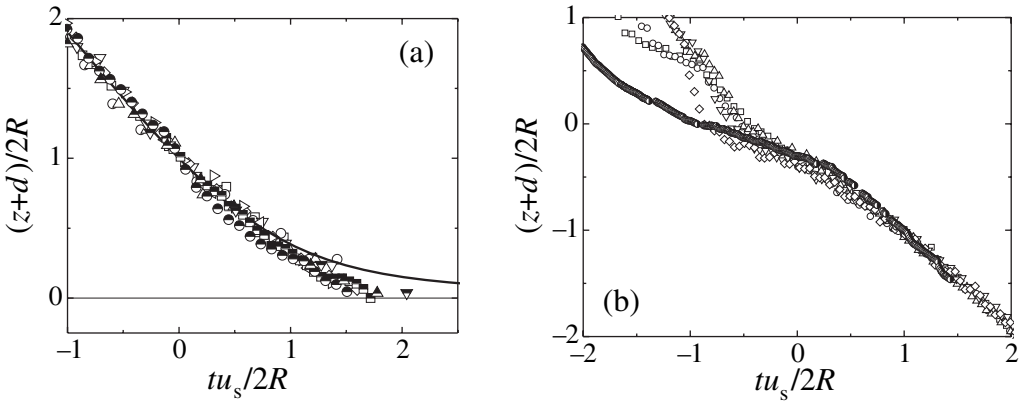

Figure 9. Dimensionless master curves scaling for the approach (a) and departure (b) stages for spheres in System IA (semi-filled symbols, $Bo = 0.05$–0.52) and System II (open symbols, $Bo = 0.32$–1.17). We set $t = 0$ as the time at which $(z+d)/2R = 1$ (approach) or -1 (moving away). The solid line in (a) represents the theoretical curve for the approach of a rigid sphere towards a non-deformable free surface.

more abundant in terms of distances covered as the high viscosity in System IA leads to long measurement times for a large spectrum of heights. As a consequence of flow, a pressure gap is created behind the sphere. As long as the capillary pressure of the deformed interface does not exceed the pressure gap behind the sphere, the interface moves along with the sphere. As gravity pulls not only the sphere but also the interface, the initial movement of the sphere is restrained. Once the pressure gap behind the sphere is insufficient to deform the interface further, the sphere detaches from the deformed interface and accelerates towards its bulk sedimentation velocity in the liquid phase. Meanwhile, the deformed interface flattens again. Making height and time dimensionless, as for the approach stage, results in master curves for separations between the sphere and the interface smaller than $z+d = 0$, as shown in figure 9(b). For smaller values of $z+d$, the curves are steeper for larger spheres, for which the gravitational force is large compared to the capillary forces.

5. V-mode

We observe a crossover regime in between the drainage and tailing transport configurations at moderate Bond numbers of ∼2–3. After transport the sphere leaves the interface behind with a characteristic V-shape, and so we refer to it as the V-mode. In this regime, the gravitational force dominates over the capillary force, but the capillary force does play a role. A characteristic image sequence for transport through the V-mode is shown in figure 10 for System IB. The V-mode was also observed in System III. The transport stages of the V-mode may be divided into several more or less consecutive events, which are schematically shown in figure 11(a). Initially the sphere sediments at constant velocity in the colloidal gas phase (1A). Close to the interface the sphere slows down due to solvent backflow (1B) and the interface strongly deforms on approach of the sphere (1C). While the sphere gradually moves through the interface, a gas phase film persists around the sphere well in the liquid phase. Several connections are formed

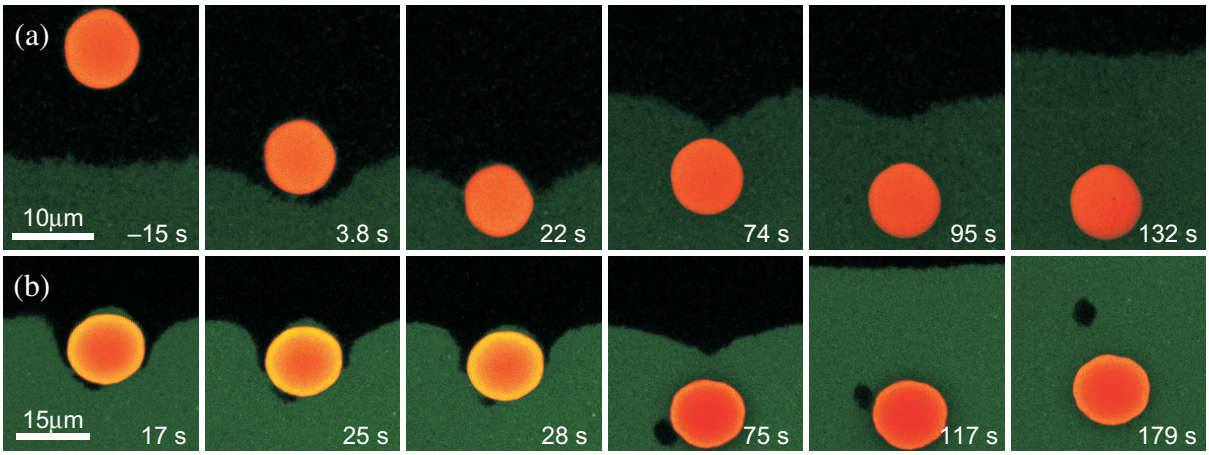

Figure 10. (a) Transport through the V-mode in System IB for a 9.6 μm diameter sphere with $Bo = 2.0$. The time at which the sphere centre reaches the position of the undeformed interface is set as $t = 0$. We use the same labelling in the text. (b) Image series similar to (a) for a 15.2 μm diameter sphere ($Bo = 4.9$). Several connections are formed between the interface and the wetting film on the sphere, resulting in the entrapment of gas bubbles. See Movie 4, available at stacks.iop.org/NJP/12/023013/mmedia.

in quick succession between the deformed interface and the wetting film of colloidal liquid on the sphere (2A), with the sphere still relatively close to the interface. The creation of the connections is likely mediated by capillary waves, on both the deformed interface and the wetting film on the sphere. In most cases, the first connection is made at the bottom part of the sphere, slightly shifted from the centre of deformation. Then a second connection forms at the free, non-coupled side of the sphere and even more connections may be formed at other free parts of the sphere surface. The gas phase film around the sphere is ruptured at several locations around the sphere due to the formation of multiple connections. Next, these connections grow (2B), thereby entrapping 'bubbles' of polymer-rich phase (2C), as visualized in great detail in figure 10(b). Note that due to confocal slicing not all formations of connections—or bubbles—can be observed in these two-dimensional measurements. Meanwhile, the distortion of the interface reaches over a few sphere diameters along the interface. This gas phase gap above the sphere then decreases its width (2D) and, when the top of the sphere equals the maximum interfacial deformation, it disconnects from the interface that has attained a characteristic V-shape (2E). The sphere speeds up in the liquid phase (3A) and the interface further restores towards its initial flat shape (3B). In time, as the sphere sediments downward, the gas bubbles flow along the sphere surface (3C) and detach from it (3D). The sphere moves further in the bulk liquid phase and reaches a constant velocity (3E). Initially, the bubbles are in the pressure gap behind the sphere and are dragged along, but eventually move upward with a velocity increasing up to a constant velocity. The bubbles ultimately coalesce with the bulk gas phase at the interface (3F), as extensively described in [39].

When the top of the sphere has reached the height of the undeformed interfacial position, the interface has not fully recovered yet, and the sphere leaves a V-shaped interfacial profile behind. Note that this is slightly different from the sphere that drags the interface along in the drainage mode. In the latter case, the interface has fully recovered by the time the sphere is

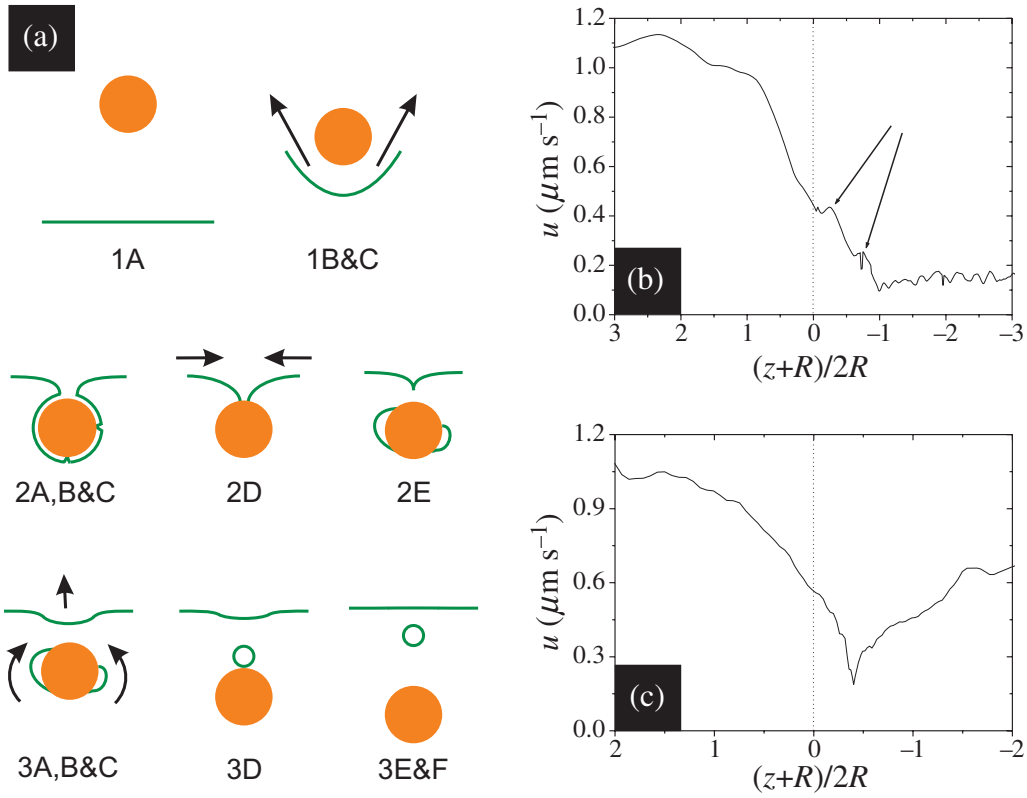

Figure 11. (a) Subdivision of the (1) approach, (2) transport and (3) moving-away stages in events for the V-mode. The same labelling is used in the text. (b) V-mode velocity profile during transport of the 9.6 μm diameter sphere ($Bo = 2.0$) in System IB shown in figure 10(a). The two tiny peaks in velocity coincide with film rupture events. (c) Similar to (b) for a 14.6 μm diameter sphere ($Bo = 3.2$) in System III with a much more pronounced increase in velocity after transport of the sphere.

fully below the undeformed interfacial position, but deforms again through the pressure gap behind the sphere. In the V-mode, the recovery of the interface initially takes place by lateral fluid motion and is driven by the hydrostatic pressure imbalance between the gas phase in the V-shaped neck and the liquid phase around it. Minimization of the interfacial area drives the interfacial restoration only after the sides of the neck join by coalescence.

The film in between the sphere and the interface ruptures much earlier in System IA than in System II due to the larger interface roughness. Despite the very different value of μ, the transition to the tailing mode takes place at similar Bond numbers for both systems ($Bo \sim 3$).

Two representative velocity profiles throughout the V-mode transport process are shown in figure 11(b) and (c) as a function of $z + R$ for Systems IA and III. For the V-mode, the velocity clearly reduces close to the interface. In figure 11(b), two tiny peaks are subsequently observed, which coincide with the observed formation and growth of connections between the deformed interface and the wetting film around the sphere, as shown in detail in figure 10(a). For the drainage transport configuration, the maximum velocity was well described by $u_c/3$. At this state point, $u_c/3 = 0.10\,\mu\mathrm{m\,s^{-1}}$, which is significantly larger than the observed increases in

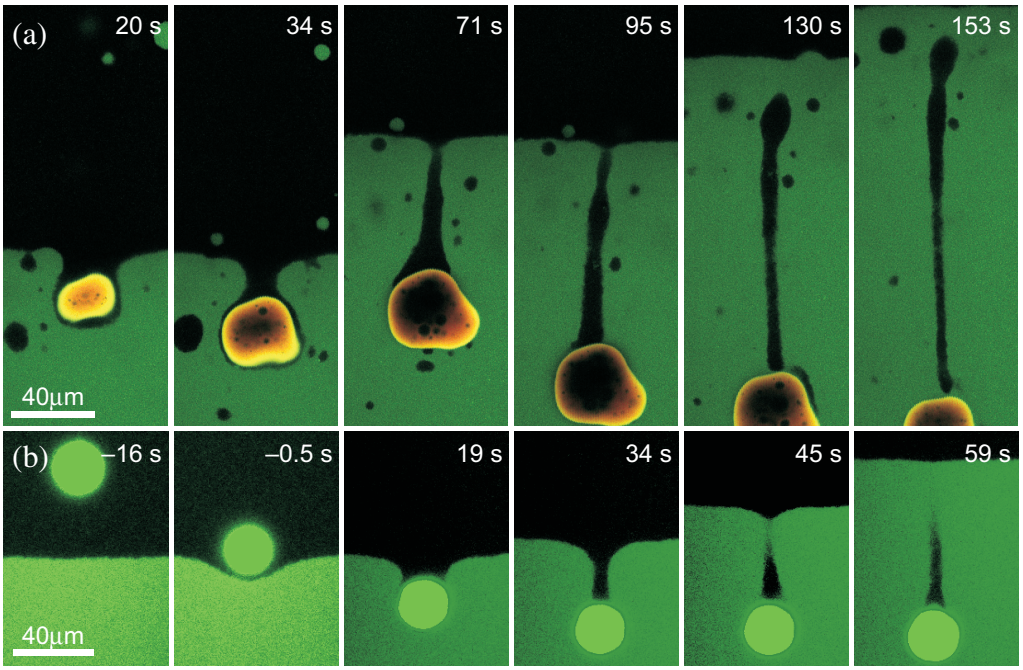

Figure 12. Transport through the tailing configuration for (a) a 40 μm sphere-like object ($Bo = 34$) in System IB and (b) a 24 μm diameter sphere ($Bo = 9$) in System III. The time at which the sphere centre reaches the position of the undeformed interface is set as $t = 0$. The sphere leaves a long column of colloidal gas behind. See Movie 5, available at stacks.iop.org/NJP/12/023013/mmedia.

velocity. This supports the scenario of a more dominant gravitational force and multiple rupture events in quick succession at the sides of the sphere, potentially partly negating each other. Due to the high viscosity contrast between the phases, the bulk sedimentation velocity in the colloidal liquid is quite low. Therefore, the increase in velocity after transport of the sphere is relatively small. In figure 11(c), increases in velocity due to rupture of the gas phase film are not observed. Here, the capillary velocity is larger, $u_c/3 = 1.5\,\mu\mathrm{m\,s^{-1}}$, but the sedimentation velocities are larger as well. Moreover, the reduced resolution in time, the identical dyes of the sphere and the colloids and the smaller interfacial roughness hinder the observation of rupture events. The film rupture events take place more or less at the side of the sphere, and capillary forces hardly contribute to the downward velocity, which is representative for all spheres in this system. In figure 11(c), the increase in velocity after passage of the interface is much more pronounced, due to a lower μ, than in figure 11(b). The observation of the V-mode emphasizes the tunability of our experimental system by bridging the low (drainage) and high (tailing) Bond number limits, where either capillary or gravitational forces dominate the transport of the sphere through the interface.

6. Tailing mode

At values of $Bo > 4$, we observe that spheres move through the colloidal gas–liquid interface via the tailing transport configuration: after transport the sphere leaves a column or 'tail' of colloidal gas phase behind. Figures 12(a) and (b) show images of the transport process for a 40 μm

sphere-like object (System IB, $Bo = 34$) and for a 24 μm diameter sphere (System III, $Bo = 9$). The events taking place in the tailing regime during the approach, transport, moving-away and column break-up stages, which we describe consecutively, are sketched in figure 14(a). All events are clearly observable; however, the order of the events and the extent to which they take place may vary, depending on the dimensionless parameters Bo, β and μ, and $\sqrt{\langle h^2 \rangle}$. During the approach stage the spheres initially sediment at constant velocity through the gas phase (1A). At a sphere-interface spacing of $\sim$1–2 times, the sphere diameter of the interface starts to deform (1B) and the sphere slows down due to solvent backflow (1C). The deformation of the interface increases strongly upon further approach of the sphere. Subsequently, as the sphere passes through the interface, it entrains a film of the polymer-rich phase around it and a column of the same material behind it. The polymer-rich film around the sphere thins (2A) and thereby feeds the column of polymer-rich material. While the sphere is fully immersed in the colloid-rich phase, several connections are formed nearly simultaneously between the wetting film of colloid-rich material on the sphere and the bulk colloid-rich phase (2B). The connections grow rapidly (2C), but the net capillary force on the sphere is negligible as no sudden increase in velocity is observed. Because of the rupture of the gas film, gas 'bubbles' are entrapped by the liquid phase around the sphere surface (2D). The sphere is completely immersed in the liquid phase and leaves a tail of gas phase material behind (3A). As the sphere sediments further and speeds up in the liquid phase, the column elongates and thins. After rupture of the film, the created gas bubbles flow around the sphere surface and coalesce with the gas column (3B). The sphere detaches from the column (3C) when the width of the column just above the sphere becomes sufficiently small to be bridged by thermal fluctuations—present at the gas–liquid interface of the column. The sphere sediments further at constant velocity in the bulk liquid phase (3D) and usually still releases a few gas bubbles after detachment from the column (3E). During the final stage of the transport process, the gas column breaks up through a Rayleigh–Plateau instability [40, 41], similar to [32]. This instability is driven by the interfacial tension and reduces the total surface area of a fluid thread by breaking it into drops. Figure 13 shows two image series for column break-up. First, the liquid phase encloses the column due to the closure of the interface above the column (4A), which is probably caused by the high Laplace pressure of the locally curved interface. This starts well before the column has reached its maximum length. Undulations arise at the interface between the gas column and the bulk liquid phase (4B). At some positions along the column its width becomes small enough to be bridged by a connection between both sides of the column. This is mediated by capillary waves on the interface of the column and the colloid-rich phase. The gas column is ruptured and breaks up into bubbles (4C). Eventually, the gas bubbles move upward towards the interface (4D) and coalesce with the bulk gas phase at the interface (4E), as in [39]. The confocal slicing method sometimes obscures certain events, as can be seen in some of the images of figures 12(a) and (b). In principle, this can be solved by sufficiently fast 3D confocal microscopy or by optical microscopy at somewhat lower resolution.

The observed break-up pattern is strongly reminiscent of the break-up of threads at ultralow interfacial tension [32, 42], with for example the absence of satellite droplets. The only difference with these studies is that here the surrounding fluid is the more viscous phase. The break-up of the column after transport for a 18.8 μm sphere in System IB with $Bo = 7.5$ is shown in figure 13(a) and results in only three droplets, apart from an additional droplet that is released from the surface of the sphere. The break-up in figure 13(b) in System III stretches beyond the measurement time but clearly results in a larger amount of droplets. Clearly, both

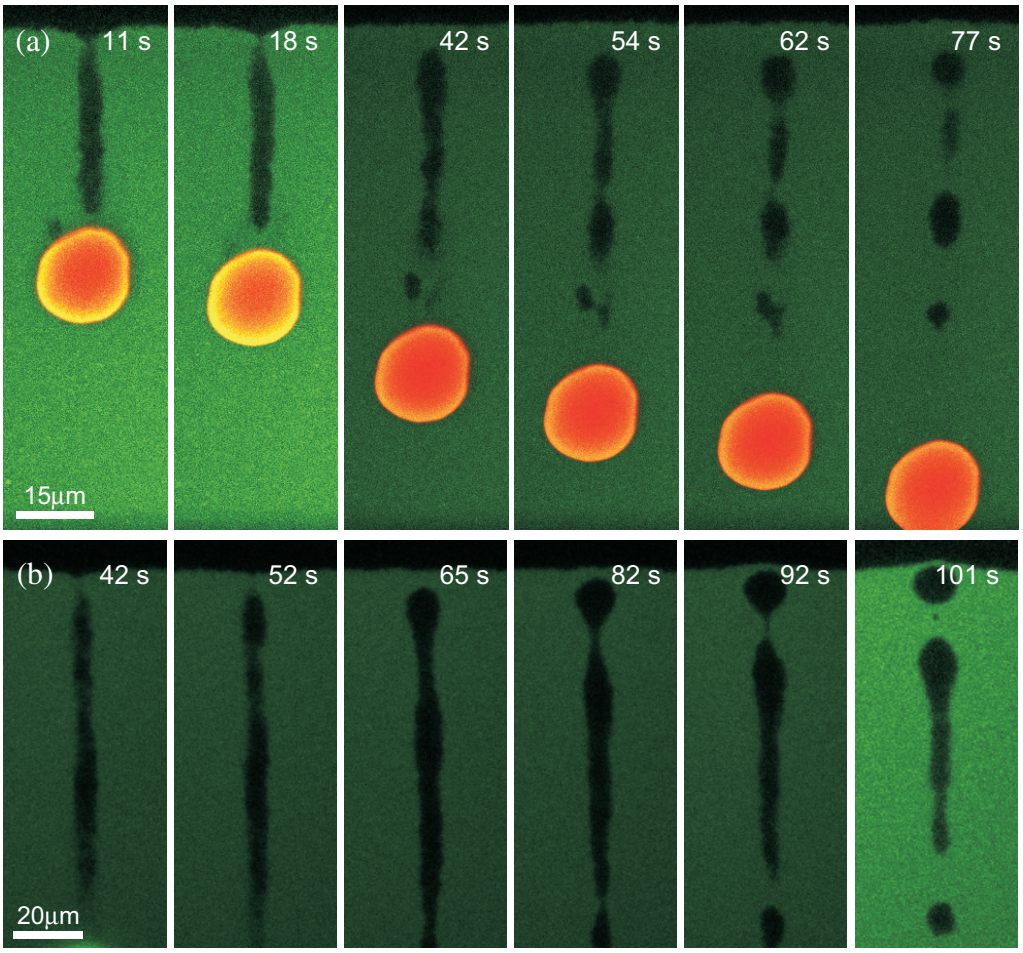

Figure 13. Break-up of gas columns after transport of spheres with a diameter of (a) 18.8 μm ($Bo = 10$) in System IB with time set relative to the detachment of the sphere from the column (see Movie 7, available at stacks.iop.org/NJP/12/023013/mmedia) and (b) 24 μm ($Bo = 5$) in System III, depicted in figure 12(b), for which we set $t = 0$ when the sphere centre has reached the undeformed interface position. (See Movie 6, available at stacks.iop.org/NJP/12/023013/mmedia.) The column breaks up into several gas bubbles that eventually coalesce with the interface.

the lower viscosity ratio μ and the smaller thermal roughness may play a role here. A decreased viscosity ratio increases the extent of interfacial deformation, while the thermal roughness affects the final length of the column and the width at which the column breaks up.

Figure 14(b) shows a representative velocity profile of the tailing transport process as a function of distance to the interface. The curve shows a clear decrease in velocity on approaching the interface, while the minimum velocity of the sphere occurs approximately a diameter below the interface. No effect of interfacial events on the velocity of the sphere is observed in either system. Finally, the spheres accelerate towards their bulk sedimentation velocity in the colloid-rich phase.

Figure 15 shows a quantitative analysis of the sphere height in time, for spheres with $Bo > 1$ transported through either the V-configuration or the tailing configuration. The spheres

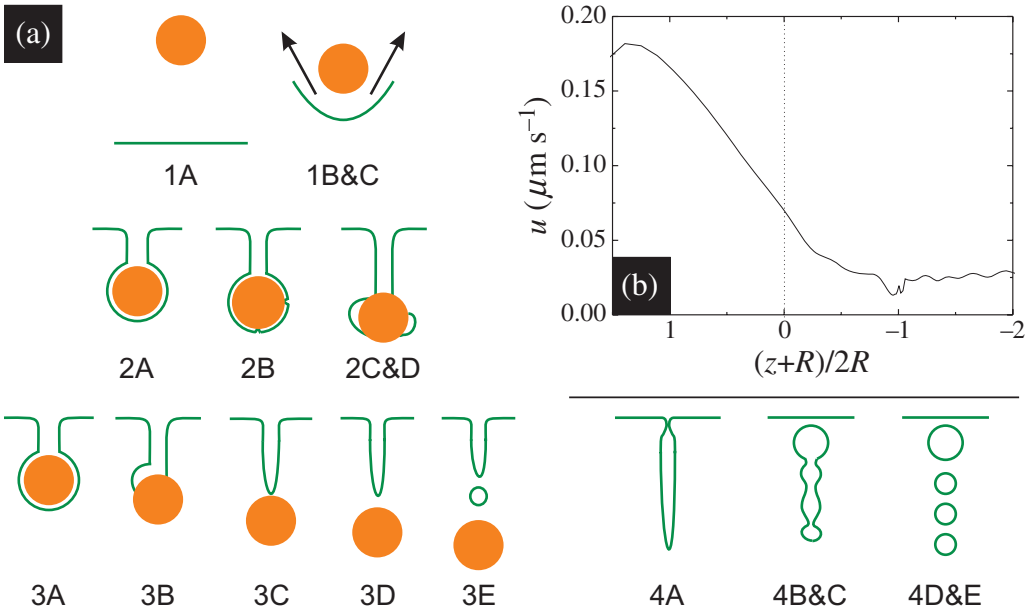

Figure 14. (a) Subdivision of the (1) approach, (2) transport (3) moving away and (4) column break-up stages in events for the tailing mode. The same labelling is used in the text. (b) Tailing velocity profile during transport of a 13.3 μm diameter sphere ($Bo = 5.1$) in System IB.

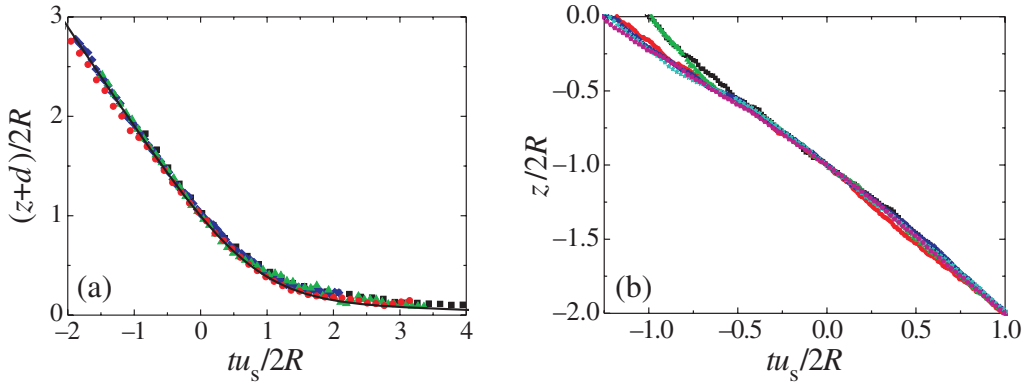

Figure 15. Dimensionless master curves scaling for the approach (a) and departure (b) stages for the transport of spheres in System IB with Bo varying from 2.0 to 5.1 (9.1–14.6 μm diameter). We set $t = 0$ as the time at which $(z + d)/2R = 1$ (approach) or -1 (moving away). The approach curves agree remarkably well with the solid line, representing the theoretical curve for the approach of a sphere towards a non-deformable free surface.

slow down considerably on approaching the interface. Although the interface deforms more than half the sphere diameter, the dimensionless approach curve for spheres of varying size, depicted in figure 15(a), still agrees remarkably well with the equation for a non-deformable free interface. For the transport stage, neither gravity nor interfacial tension is dominant such that the curves are unique for every case and therefore not scalable. The moving away of the sphere from the interface is shown in figure 15(b) for spheres of varying size and, consequently, Bo.

The curves are made dimensionless, but close to the interface neither scaling behaviour nor a systematic trend as a function of particle diameter is observed. Possibly the creation of bubbles during the rupture of the gas phase film affects the acceleration profile in a way that is not captured in the scaling. However, further away from the interface, that is $\frac{z}{2R} < -\frac{1}{2}$, scaling is observed.

2D confocal microscopy is not particularly well suited to quantitative studies of the break-up of the gas column. From an image the local width of the column can be determined with high accuracy, but confocal slicing causes the true diameter of the column to be frequently out of focus. Optical microscopy is a better candidate for capturing the full break-up, such as in [32], but reduces the lateral resolution. Fast 3D confocal microscopy is an alternative, but is experimentally challenging.

7. Conclusion

We have presented quantitative microscopy experiments, visualizing in detail all events involved in the transport of a wettable sphere through a colloidal fluid–fluid interface in the low Reynolds regime. Due to the ultralow interfacial tension and the use of polydisperse rigid spheres, we were able to observe different transport regimes within our experimental system in real time and real space. The sphere passes through the interface via the *drainage* transport configuration at low Bond numbers, i.e. a dominant capillary force. Gravity dominates at high Bond numbers and the *tailing* configuration is observed. We are able to understand the velocity profile of the sphere as a function of height through scaling arguments and a simple force balance, which reveals the capillary forces acting on the sphere. Furthermore, the thermal interface roughness was visualized and found to influence the passage of the sphere through the interface; the connection between the sphere and the interface is, for instance, clearly mediated by capillary waves. This work's visual detail and quantitative understanding may prove helpful in the understanding of the transport of solid particles in similar processes that take place in a wide range of bio- and geophysical systems.

Acknowledgments

It is our pleasure to thank Chantal Vonk, Roel Dullens, Stefano Sacanna, Bonny Kuipers and Emile Bakelaar for help with the synthesis and characterization of the experimental system. This work was supported by the Stichting voor Fundamenteel Onderzoek der Materie (FOM), which is part of the Nederlandse Organisatie voor Wetenschappelijk Onderzoek (NWO). Support of VWAdV by the DFG through the SFB TR6 is acknowledged.

References

[1] Phillips L F 2004 *Acc. Chem. Res.* **37** 982–8
[2] Shin W T, Yiacoumi S and Tsouris C 2004 *Curr. Opin. Colloid Interface Sci.* **9** 249–55
[3] Stechemesser H J and Nguyen A V 1999 *Int. J. Miner. Process.* **56** 117–32
[4] Lande R and Wood A M 1987 *Deep-Sea Res.* **34** 61–72
[5] Manga M, Stone H A and O'Connell R J 1993 *J. Geophys. Res.* **98** 19979–90
[6] Bergmann R, van der Meer D, Stijnman M, Sandtke M, Prosperetti A and Lohse D 2006 *Phys. Rev. Lett.* **96** 154505

[7] Geller A S, Lee S H and Leal L G 1996 *J. Fluid Mech.* **169** 27–69
[8] Aarts D G A L 2007 *Soft Matter* **3** 19–23
[9] Aarts D G A L and Lekkerkerker H N W 2008 *J. Fluid Mech.* **606** 275–94
[10] Maru H C, Wasan D T and Kintner R C 1971 *Chem. Eng. Sci.* **26** 1615–28
[11] Shah S T, Wasan D T and Kintner R C 1972 *Chem. Eng. Sci.* **27** 881–93
[12] Pitois O, Moucheront P and Weill C 1999 *C. R. Acad. Sci., Paris* IIb **327** 605–11
[13] Srdic-Mitrovic A N, Mohamed N A and Fernando H J S 1999 *J. Fluid Mech.* **381** 175–98
[14] Abaid N, Adalsteinsson D, Agyapong A and McLaughlin R M 2004 *Phys. Fluids* **16** 1567–80
[15] Hartland S 1968 *J. Colloid Interface Sci.* **26** 383
[16] Hartland S 1969 *Chem. Eng. Sci.* **24** 987
[17] Manga M and Stone H A 1995 *J. Fluid Mech.* **287** 279–98
[18] Probstein R F 2003 *Physicochemical Hydrodynamics* (New York: Wiley)
[19] Akers B and Belmonte A 2006 *J. Non-Newton. Fluid Mech.* **135** 97–108
[20] De Gennes P G 1979 *Scaling Concepts in Polymer Physics* (Ithaca, NY: Cornell University Press)
[21] Rowlinson J S and Widom B 1982 *Molecular Theory of Capillarity* (Oxford: Clarendon)
[22] Asakura S and Oosawa F 1954 *J. Chem. Phys.* **22** 1255
[23] Vrij A 1976 *Pure Appl. Chem.* **48** 471
[24] Lekkerkerker H N W, Poon W C K, Pusey P N, Stroobants A and Warren P B 1992 *Europhys. Lett.* **20** 559
[25] Vliegenthart G A and Lekkerkerker H N W 1997 *Prog. Colloid Polym. Sci.* **105** 27
[26] de Hoog E H A and Lekkerkerker H N W 1999 *J. Phys. Chem.* B **103** 5274
[27] Chen B H, Payandeh B and Robert M 2000 *Phys. Rev.* E **62** 2369
[28] Aarts D G A L, van der Wiel J H and Lekkerkerker H N W 2003 *J. Phys.: Condens. Matter* **15** S245
[29] Aarts D G A L, Schmidt M and Lekkerkerker H N W 2004 *Science* **304** 847
[30] Butt H J 1994 *J. Colloid Interface Sci.* **166** 109–17
[31] Zhang L, Ren L and Hartland S 1996 *J. Colloid Interface Sci.* **180** 493–503
[32] Hennequin Y, Aarts D, van der Wiel J H, Wegdam G, Eggers J, Lekkerkerker H N W and Bonn D 2006 *Phys. Rev. Lett.* **97** 44502
[33] Happel J and Brenner H 1986 *Low Reynolds Number Hydrodynamics* (Dordrecht: Martinus Nijhoff)
[34] Bosma G, Pathmamanoharan C, de Hoog E H A, Kegel W K, van Blaaderen A and Lekkerkerker H N W 2002 *J. Colloid Interface Sci.* **245** 292
[35] Vincent B 1990 *Colloids Surf.* **50** 241
[36] Aarts D G A L 2005 *J. Phys. Chem.* B **109** 7407
[37] Hennequin Y, Aarts D G A L, Indekeu J O, Lekkerkerker H N W and Bonn D 2008 *Phys. Rev. Lett.* **100** 178305
[38] de Villeneuve V W A, Aarts D G A L and Lekkerkerker H N W 2006 *Colloids Surf.* A **282** 61–7
[39] Aarts D G A L, Lekkerkerker H N W, Guo H, Wegdam G H and Bonn D 2005 *Phys. Rev. Lett.* **95** 164503
[40] Tomotika S 1935 *Proc. R. Soc.* A **150** 322
[41] Tomotika S 1936 *Proc. R. Soc.* A **153** 302–18
[42] Moseler M and Landman U 2000 *Science* **289** 1165